JOURNAL OF SOLID STATE CHEMISTRY **122,** 59–67 (1996)
ARTICLE NO. 0082

Thermal Behavior and Crystal Structure of Ceric and Cerous Rubidium Nitrates

N. Guillou, J. P. Auffrédic, and D. Louër

Laboratoire de Cristallochimie (CSIM, URA CNRS 1495), Avenue du Général Leclerc, 35042 Rennes Cedex, France

Received July 12, 1995; in revised form November 13, 1995; accepted November 14, 1995

The crystal structures of ceric rubidium nitrate, $Ce^{IV}Rb_2(NO_3)_6$, and cerous rubidium nitrate, $Ce_2^{III}Rb_3(NO_3)_9$, were refined from their X-ray powder diffraction data. Their decomposition process was revealed by means of temperature-dependent X-ray diffraction (TDXD) and TG-DSC analyses. The thermal decomposition of $Ce^{IV}RB_2(NO_3)_6$ is characterized by the Ce(IV) → Ce(III) → Ce(IV) reduction–oxidation sequence. The decomposition scheme depends on the environmental atmosphere as well as the mechanical treatment of the precursor. The first stages of the decomposition proceed through the formation of a mixture of phases consisting of $RbNO_3$, CeO_2, $Ce_2^{III}Rb_3(NO_3)_9$, and a new phase with the suggested formula $Ce^{III}Rb(NO_3)_4$. This last compound is also an intermediate phase observed in the decomposition of $Ce_2^{III}Rb_3(NO_3)_9$. $Ce^{III}Rb(NO_3)_4$ melts at 190°C and decomposes into $RbNO_3$ and CeO_2.

INTRODUCTION

Aqueous solutions of ceric compounds are well known for their oxidation properties and hexanitrato ammonium cerate, $Ce^{IV}(NH_4)_2(NO_3)_6$, was proposed long ago as the reference standard in oxidimetry (1). The reaction of oxidation by the Ce(IV) cation can occur only not in aqueous media but also in the solid state. Recently, we have clearly demonstrated that two successive changes of the oxidation state of cerium are observed when cerium potassium nitrate $Ce^{IV}K_2(NO_3)_6$ is heated (2, 3). As shown from temperature-dependent X-ray powder diffraction (TDXD), the first stage of the decomposition of this compound is characterized by the simultaneous formation of the cerous compound $Ce_2^{III}K_3(NO_3)_9$, together with CeO_2 and KNO_3, which involves the oxidation of oxygen atoms of the nitrate groups. The final product of this decomposition is CeO_2. This Ce(IV) → Ce(III) → Ce(IV) reduction–oxidation sequence had been observed earlier for the thermal decomposition of $(NH_4)_4Ce^{IV}(SO_4)_4 \cdot 2H_2O$ (4, 5), $Ce(SO_4)_2 \cdot 4H_2O$ (6), and various cesium cerium sulfates (7) and, also, recently for that of $Ce^{IV}(NH_4)_2(NO_3)_6$ (8). For the last compound, the occurrence of a Ce(III) phase was proved by XPS and magnetic susceptibility measurements and was explained by the reducing effect of ammonium ions. In fact, as evidenced by our results, this feature is not typical of these ammonium compounds. On the other hand, it was not observed during the thermal decomposition of $Ce^{IV}Mg(NO_3)_6 \cdot 8H_2O$ (9). Therefore, the question arises as to whether this phenomenon can occur for other ceric nitrate salts $CeM_2(NO_3)_6$, where M is a monovalent cation. The present study deals with the crystal structures and the thermal decomposition mechanisms of $Ce^{IV}Rb_2(NO_3)_6$ and $Ce_2^{III}Rb_3(NO_3)_9$.

EXPERIMENTAL

Sample Preparation

$Ce^{IV}Rb_2(NO_3)_6$ was obtained at 40°C, in the form of small orange crystals, from a solution of stoichiometric quantities of ceria and rubidium nitrate in concentrated nitric acid. Reactive hydrous ceria was prepared, as described elsewhere (10). The mixture of this hydrous oxide and rubidium nitrate was then completely soluble in concentrated nitric acid boiling in a closed vessel. The Ce^{4+} content was determined by titration with Mohr's salt, and the NO_3^- content by the Dewarda method. The experimental values (%) are given first, followed by the theoretical values in brackets: 20.8 [20.51] and 54.6 [54.46], respectively. They confirm the chemical formula $Ce^{IV}Rb_2(NO_3)_6$, reported long ago (11). $Ce_2^{III}Rb_3(NO_3)_9$ was synthesized, as small colorless crystals, by evaporation at 40°C of an aqueous solution of stoichiometric quantities of cerium (III) nitrate and rubidium nitrate.

For thermal and X-ray diffraction studies, the materials were ground in cyclohexane, for times ranging from 3 to 60 min, by using a micronizing mill from McCrone research associated LTD.

0022-4596/96 $18.00

TABLE 1
Details of the Rietveld Refinement for Ceric and Cerous Rubidium Nitrates

	$Ce^{IV}Rb_2(NO_3)_6$	$Ce_2^{III}Rb_3(NO_3)_9$
a (Å)	13.0567(5)	13.8411(4)
b (Å)	6.8684(2)	
c (Å)	8.1786(3)	
β (°)	91.436(4)	
V (Å^3)	733.22(3)	2651.6(2)
Space group	$P2_1/n$	$P4_132$
Z	2	8
Wavelength (Å)	1.54059	1.54059
2θ range (°)	10–100	13–120
No. of reflections	790	438
No. of structural parameters	45	29
No. of profile parameters	15	13
No. of atoms	14	9
R_F	0.04	0.06
R_B	0.05	0.06
R_p	0.06	0.06
R_{wp}	0.07	0.08

X-Ray Powder Diffraction

X-ray powder diffraction data were collected with a D500 Siemens powder diffractometer using the Bragg–Brentano geometry and operating with pure Cu$K\alpha_1$ radiation (λ = 1.54059 Å), whose features were reported elsewhere (12). The alignment of the diffractometer was checked by means of standard reference materials and the zero error was measured as less than 0.005°(2θ). For $Ce^{IV}Rb_2(NO_3)_6$, a top-loading sample holder was used and the diffraction pattern was scanned over the range 10°–100°(2θ) with a step length of 0.02°(2θ) and a counting time of 31 sec step^{-1}. For $Ce_2^{III}Rb_3(NO_3)_9$, the sample was kept in a nitrogen atmosphere by using a tight sample holder to prevent its transformation. The powder diffraction pattern was scanned over a range 8–120°(2θ) with a step length of 0.02°(2θ) and a counting time of 28 sec step^{-1} from 8.00° to 64.50°(2θ) and 56 sec step^{-1} from 64.52° to 120.00°(2θ). Then, the full pattern was scaled to the lower counting time.

Temperature-dependent X-ray powder diffraction (TDXD) was carried out with an INEL (CPS 120) curved position-sensitive detector (PSD). The PDS was used in a semifocusing geometry by reflection, with a monochromatic Cu$K\alpha_1$ radiation, as previously described (13). The stationary powder sample is located at the center of the goniometer in a monitored high-temperature device (Rigaku). To ensure satisfactory counting statistics a counting time of 3000 sec per pattern was selected.

Thermogravimetry and Differential Scanning Calorimetry

Simultaneous TG and DSC analyses were carried out using a Rigaku Thermoflex TG-DSC instrument. When only the TG run is recorded, powdered samples of about 20 mg were spread evenly in a large sample holder in order to avoid mass effects and the same thermal conditions as used in TDXD were reproduced.

STRUCTURE REFINEMENT OF $Ce^{IV}Rb_2(NO_3)_6$ AND $Ce_2^{III}Rb_3(NO_3)_9$ FROM X-RAY POWDER DIFFRACTION

Indexing of Powder Diffraction Patterns

The indexing of powder diffraction patterns by the program DICVOL91 (14) gave a monoclinic solution for $Ce^{IV}Rb_2(NO_3)_6$ and a cubic solution for $Ce_2^{III}Rb_3(NO_3)_9$. The powder diffraction data were reviewed by means of the computer program NBS*AIDS83 (15). The parameters of the two unit cells are reported in Table 1. The cell parameters of $Ce^{IV}Rb_2(NO_3)_6$ compare well with those of $Ce^{IV}(NH_4)_2(NO_3)_6$ (16) [a = 13.069(3), b = 6.8461(2), c = 8.1732(16) Å, β = 91.36(2)°] and of the monoclinic form of $Ce^{IV}K_2(NO_3)_6$ (17) [a = 12.707(1), b = 6.6858(6), c = 8.2535(7) Å, β = 91.547(8)°]. This result shows that these compounds are isostructural. Likewise, $Ce_2^{III}Rb_3(NO_3)_9$ [a = 13.8411(4) Å] and $Ce_2^{III}K_3(NO_3)_9$ [a = 13.5975(8) Å] (18) have similar parameters and can be considered as isostructural.

Refinement of the Structures

Atomic coordinates of $Ce^{IV}(NH_4)_2(NO_3)_6$ and $Ce_2^{III}K_3(NO_3)_9$ were used as initial structural parameters in the refinement, from X-ray powder diffraction data, of the structures of $Ce^{IV}Rb_2(NO_3)_6$ and $Ce_2^{III}Rb_3(NO_3)_9$, respectively. These starting positions were refined with the Rietveld refinement program FULLPROF (19). For both cases, a pseudo-Voigt function was selected to describe individual line profiles and the usual quadratic form in tan θ was used to describe the angular dependence of peak widths. Details of refinements are summarized in Table 1.

For $Ce^{IV}Rb_2(NO_3)_6$, the final Rietveld refinement was carried out in the angular range 10°–100°(2θ), since no reliable diffraction information was available at higher angles. The following parameters were involved in the final refinement: 1 scale factor, 39 atomic coordinates, 5 isotropic temperature factors, 1 zero point and 4 cell parameters, 3 half-width parameters, the line-shape factor η, and 6 coefficients to define the functional dependence of the background. In the case of $Ce_2^{III}Rb_3(NO_3)_9$, the final Rietveld refinement was carried out in the angular range 13°–120°(2θ). The final calculation involved the following parameters: 1 scale factor, 19 atomic coordinates, 9 isotropic

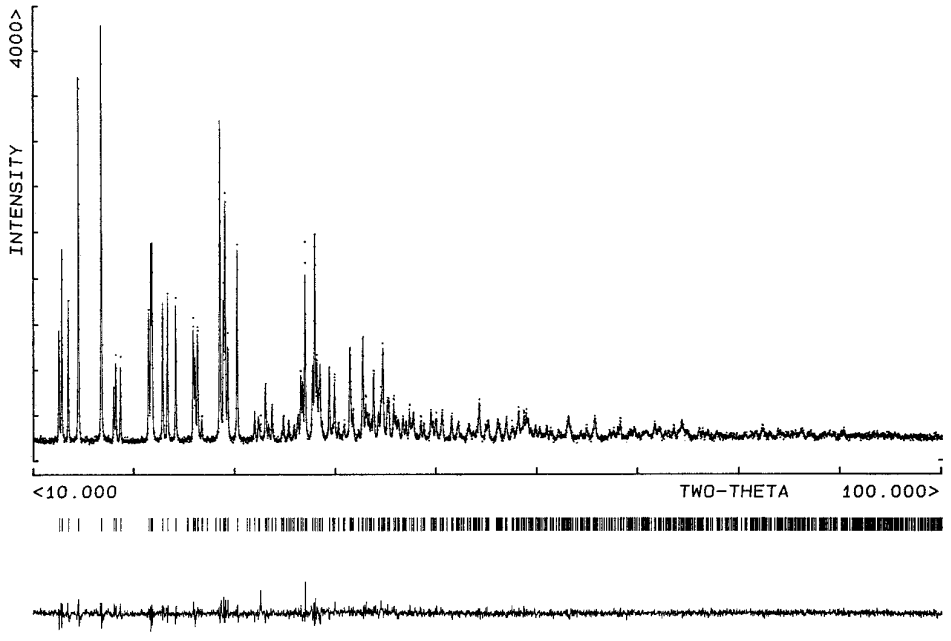

FIG. 1. The final Rietveld plot for $Ce^{IV}Rb_2(NO_3)_6$. In the upper portion, the observed data are shown by dots; the calculated pattern is displayed by solid line. The lower curve is a plot of the difference, observed minus calculated.

temperature factors, 1 zero point and 1 cell parameter, 3 half-width parameters, 1 asymmetry factor, 2 parameters to define the θ-dependent pseudo-Voigt profile shape function, and five coefficients to describe the functional dependence of the background. Figures 1 and 2 show the final fits obtained between calculated and observed patterns for $Ce^{IV}Rb_2(NO_3)_6$ and $Ce_2^{III}Rb_3(NO_3)_9$, respectively. They correspond to satisfactory crystal-structure model indicators and profile factors for the two compounds (see Table 1). Final atomic coordinates are given in Tables 2 and 3 and selected bond distances and angles in Tables 4 and 5 for $Ce^{IV}Rb_2(NO_3)_6$ and $Ce_2^{III}Rb_3(NO_3)_9$, respectively.

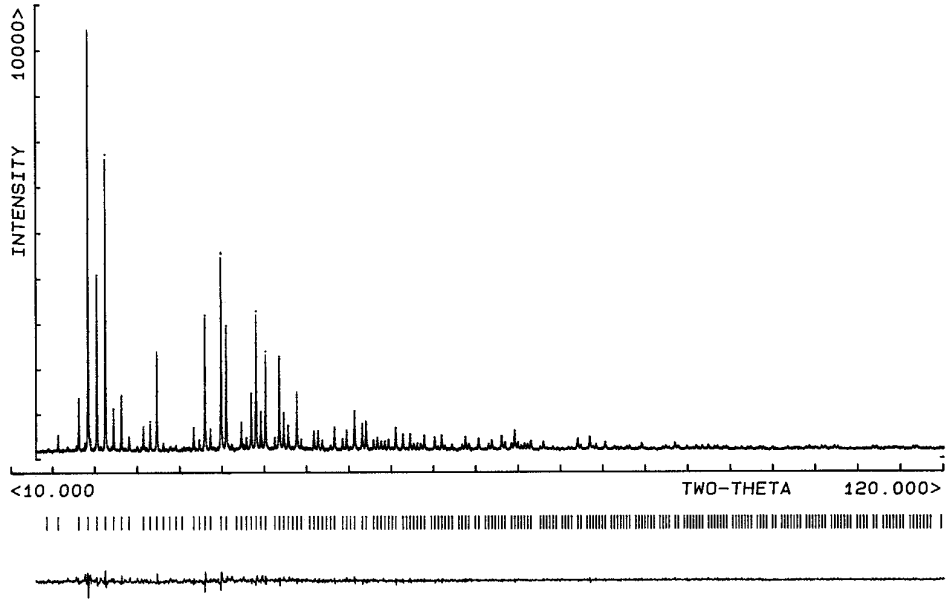

FIG. 2. The final Rietveld plot for $Ce_2^{III}Rb_3(NO_3)_9$. In the upper portion, the observed data are shown by dots; the calculated pattern is displayed by solid line. The lower curve is a plot of the difference, observed minus calculated.

TABLE 2
Final Atomic Parameters and Their Estimated Standard Deviations for $Ce^{IV}Rb_2(NO_3)_6$

Atom	x	y	z	B_{iso} (Å^2)
Ce	0.5	0.5	0.5	1.19(8)
Rb	0.1612(2)	0.2633(5)	0.5260(3)	2.2(1)
N(1)	0.683(2)	0.245(4)	0.471(2)	1.7(3)[a]
$O(1_1)$	0.619(1)	0.216(2)	0.579(2)	1.5(2)[b]
$O(1_2)$	0.666(1)	0.387(2)	0.368(2)	1.5(2)[b]
$O(1_3)$	0.746(1)	0.120(2)	0.435(2)	2.6(3)[c]
N(2)	0.389(2)	0.231(3)	0.275(3)	1.7(3)[a]
$O(2_1)$	0.486(1)	0.207(2)	0.308(2)	1.5(2)[b]
$O(2_2)$	0.345(1)	0.374(2)	0.340(2)	1.5(2)[b]
$O(2_3)$	0.340(1)	0.108(2)	0.197(2)	2.6(3)[c]
N(3)	0.444(2)	0.256(3)	0.770(3)	1.7(3)[a]
$O(3_1)$	0.403(1)	0.216(2)	0.638(2)	1.5(2)[b]
$O(3_2)$	0.494(1)	0.406(2)	0.797(2)	1.5(2)[b]
$O(3_3)$	0.437(1)	0.136(2)	0.895(2)	2.6(3)[c]

[a,b,c] Some thermal parameters are allowed to vary in the same manner.

DESCRIPTION OF THE STRUCTURES

$Ce^{IV}Rb_2(NO_3)_6$ is isostructural with $Ce^{IV}(NH_4)_2(NO_3)_6$ (16) and the monoclinic form of $Ce^{IV}K_2(NO_3)_6$ (17). The structure can be described from discrete $[Ce(NO_3)_6]^{2-}$ anions forming a "body centered" arrangement and Rb cations linked by ionic contacts. The structure of $Ce_2^{III}Rb_3(NO_3)_9$ is built from a tridimensional anionic network $[Ce_2(NO_3)_9]^{3-}$ where cerium polyhedra are linked together by bridging nitrate groups. The Rb atoms are located in the holes of the structure.

In the two structures, the cerium atoms are 12-fold coordinated and are bonded to six bidendate nitrate groups. The Ce–O distances range from 2.52(2) to 2.60(2) Å in $Ce^{IV}Rb_2(NO_3)_6$ and from 2.59(1) to 2.79(1) Å in $Ce_2^{III}Rb_3(NO_3)_9$. The mean value of 2.55 Å obtained for $Ce^{IV}Rb_2(NO_3)_6$ is in accordance with those reported for the two polymorphic forms of $Ce^{IV}K_2(NO_3)_6$ (17) (2.507 and 2.506 Å for the hexagonal and the monoclinic varieties, respectively). The mean value of Ce–O distances for $Ce_2^{III}Rb_3(NO_3)_9$ (2.67 Å) compares well with that obtained for $Ce_2^{III}K_3(NO_3)_9$ (18) (2.649 Å).

It is usual to consider a nitrate group as an unsymmetri-

TABLE 4
Selected Bond Distances (Å) and Angles (°) for $Ce^{IV}Rb_2(NO_3)_6$ with Their Standard Deviation

Within the cerium polyhedron			Around the rubidium		
Ce–$O(1_1)$	(×2)	2.56(2)	Rb–$O(1_2)$[a]		2.98(2)
Ce–$O(1_2)$	(×2)	2.56(2)	Rb–$O(1_2)$[b]		3.40(2)
Ce–$O(2_1)$	(×2)	2.55(2)	Rb–$O(1_3)$[c]		2.91(2)
Ce–$O(2_2)$	(×2)	2.54(2)	Rb–$O(2_1)$[a]		3.30(2)
Ce–$O(3_1)$	(×2)	2.60(2)	Rb–$O(2_2)$		2.97(2)
Ce–$O(3_2)$	(×2)	2.52(2)	Rb–$O(2_3)$[d]		2.99(2)
			Rb–$O(3_1)$		3.28(2)
			Rb–$O(3_2)$[e]		3.07(2)
			Rb–$O(3_3)$[e]		3.17(2)
			Rb–$O(3_3)$[f]		2.94(2)
Within the nitrate groups					
N(1)–$O(1_1)$		1.24(3)	$O(1_1)$–N(1)–$O(1_2)$		118(2)
N(1)–$O(1_2)$		1.31(3)	$O(1_1)$–N(1)–$O(1_3)$		122(2)
N(1)–$O(1_3)$		1.24(3)	$O(1_2)$–N(1)–$O(1_3)$		118(2)
N(2)–$O(2_1)$		1.30(3)	$O(2_1)$–N(2)–$O(2_2)$		117(2)
N(2)–$O(2_2)$		1.26(3)	$O(2_1)$–N(2)–$O(2_3)$		121(2)
N(2)–$O(2_3)$		1.22(3)	$O(2_2)$–N(2)–$O(2_3)$		121(2)
N(3)–$O(3_1)$		1.22(3)	$O(3_1)$–N(3)–$O(3_2)$		125(2)
N(3)–$O(3_2)$		1.24(3)	$O(3_1)$–N(3)–$O(3_3)$		120(2)
N(3)–$O(3_2)$		1.32(3)	$O(3_2)$–N(3)–$O(3_3)$		115(2)

[a] $x - 1/2, 1/2 - y, 1/2 + z$.
[b] $1 - x, 1 - y, 1 - z$.
[c] $1 - x, -y, 1 - z$.
[d] $1/2 - x, 1/2 + y, 1/2 - z$.
[e] $x - 1/2, 1/2 - y, z - 1/2$.
[f] $1/2 - x, 1/2 + y, 3/2 - z$.

TABLE 3
Final Atomic Parameters and Their Estimated Standard Deviations for $Ce_2^{III}Rb_3(NO_3)_9$

Atom	x	y	z	B_{iso} (Å^2)
Ce	0.5549(1)	0.5549(1)	0.5549(1)	1.91(7)
Rb	0.375	0.1959(2)	0.5541(2)	3.6(1)
N(1)	0.401(1)	0.427(1)	0.638(1)	3.7(6)
$O(1_1)$	0.450(1)	0.3971(8)	0.557(1)	3.4(4)
$O(1_2)$	0.4234(9)	0.504(1)	0.6776(9)	3.3(4)
$O(1_3)$	0.346(1)	0.3682(9)	0.677(1)	3.7(4)
N(2)	0.625	0.514(1)	0.764(1)	3.6(8)
$O(2_1)$	0.5950(9)	0.6020(9)	0.7456(7)	1.1(3)
$O(2_2)$	0.625	0.513(1)	0.764(1)	1.7(4)

TABLE 5
Selected Bond Distances (Å) and Angles (°) for $Ce_2^{III}Rb_3(NO_3)_9$ with Their Standard Deviation

Within the cerium polyhedron			Around the rubidium		
Ce–$O(1_1)$	(×3)	2.63(1)	Rb–$O(1_1)$	(×2)	2.97(1)
Ce–$O(1_2)$	(×3)	2.59(1)	Rb–$O(1_2)$	(×2)	3.29(1)
Ce–$O(2_1)$	(×3)	2.79(1)	Rb–$O(1_3)$	(×2)	3.00(1)
Ce–$O(2_2)$	(×3)	2.66(1)	Rb–$O(1_3)$	(×2)	2.95(1)
			Rb–$O(2_1)$	(×2)	3.07(1)
Within the nitrate groups					
N(1)–$O(1_1)$		1.37(2)	$O(1_1)$–N(1)–$O(1_2)$		118(3)
N(1)–$O(1_2)$		1.25(2)	$O(1_1)$–N(1)–$O(1_3)$		118(3)
N(1)–$O(1_3)$		1.24(2)	$O(1_2)$–N(1)–$O(1_3)$		122(3)
N(2)–$O(2_1)$	(×2)	1.31(2)	$O(2_1)$–N(2)–$O(2_1)$		116(3)
N(2)–$O(2_2)$		1.28(2)	$O(2_1)$–N(2)–$O(2_2)$	(×2)	122(3)

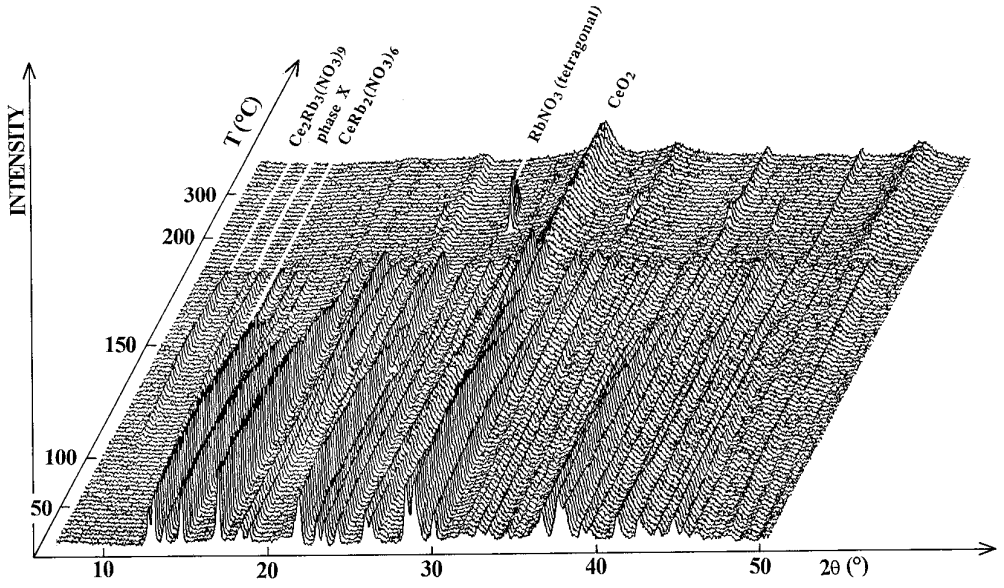

FIG. 3. TDXD plot for $Ce^{IV}Rb_2(NO_3)_6$ milled for 21 min, under nitrogen atmosphere (heating rate: 10°C h^{-1} between room temperature and 110°C, 2°C h^{-1} in the range 110–200°C, and 15°C h^{-1} in the range 200–400°C).

cal bidendate ligand when the distances from the metal atom to both coordinated oxygens differ by more than 0.2 Å (20). Although the precision on the atomic positions of the light atoms is low with regard to those of the heavy atoms, it can be noted that for $Ce^{IV}Rb_2(NO_3)_6$ the greatest difference of 0.08 Å (see Table 4) between these two distances shows that the three independent nitrate groups can be considered as bidentate symmetric. In the case of $Ce_2^{III}Rb_3(NO_3)_9$ the first nitrate group is bidentate symmetric, while the second is bidentate with regard to two cerium atoms and it bridges two icosahedra.

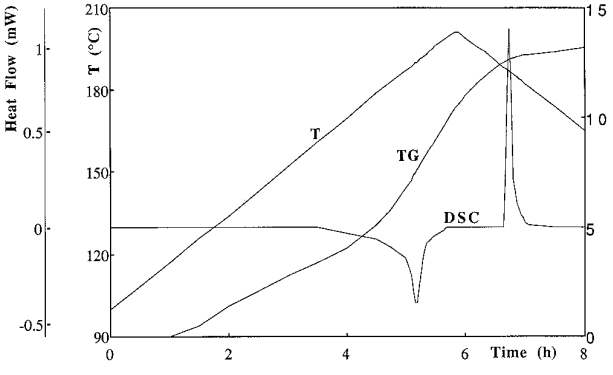

FIG. 4. Evidence of an endothermic effect on heating and an exothermic effect on cooling, observed during the decomposition of $Ce^{IV}Rb_2(NO_3)_6$ milled for 21 min, corresponding to the melting and solidification of phase *X*, respectively. The temperature (*T*) regime and TG curve are also displayed.

The rubidium ions are located between icosahedra for $Ce^{IV}Rb_2(NO_3)_6$ and in the holes of the structure for $Ce_2^{III}Rb_3(NO_3)_9$. They are surrounded by 10 oxygen atoms belonging to nitrate groups. The distances Rb–O range from 2.91 to 3.40 Å for $Ce^{IV}Rb_2(NO_3)_6$ and from 2.97 to 3.29 Å for $Ce_2^{III}Rb_3(NO_3)_9$. The rubidum atoms ensure the continuity of the structure by ionic contacts.

THERMAL BEHAVIOR OF $CE^{IV}Rb_2(NO_3)_6$

In contrast to the thermal behavior of $Ce^{IV}K_2(NO_3)_6$, described recently (3), the thermal decomposition scheme for $Ce^{IV}Rb_2(NO_3)_6$ is much more complicated. Indeed, it is sensitive to the environmental atmosphere and also to the mechanical treatment of the precursor. Three representative examples of decompositons carried out under different conditions are reported.

Thermal Decomposition in Nitrogen

Figure 3 shows the 3D representation of the successive powder diffraction patterns recorded during the thermal decomposition of a sample milled for 21 min. Similar results were obtained for other grinding times. A detailed analysis of the diffraction patterns obtained at the end of the first stage of the decomposition revealed that the solid formed is a mixture of cerium oxide, the cerous compound $Ce_2^{III}Rb_3(NO_3)_9$, and an unidentified phase (named *X*). Therefore, this first stage proceeds through the same redox reaction as observed during the decomposition of Ce^{IV}

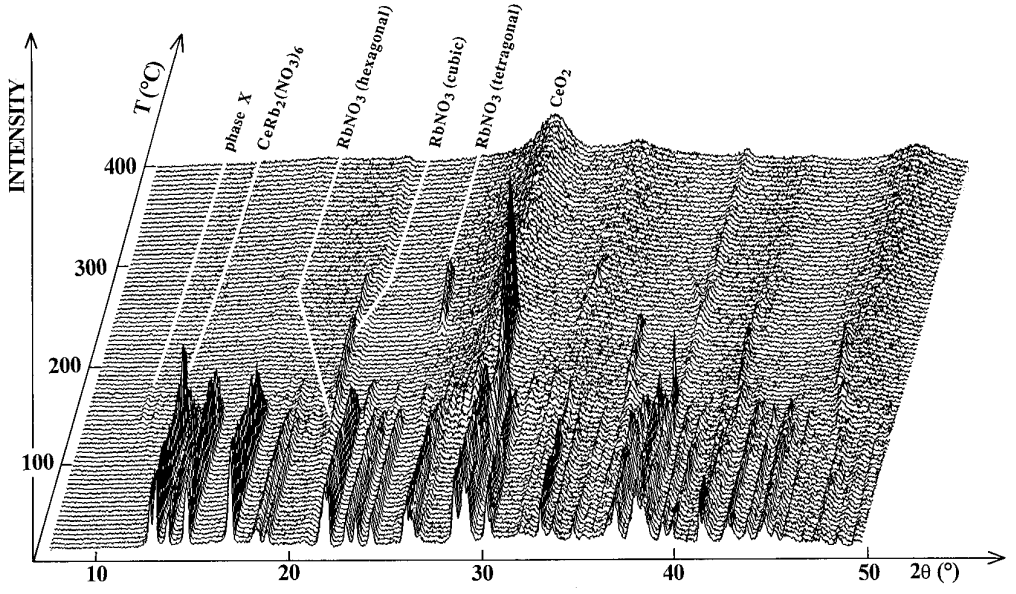

FIG. 5. TDXD plot for $Ce^{IV}Rb_2(NO_3)_6$ milled for 13 min, in vacuum (heating rate: 5°C h^{-1}).

$K_2(NO_3)_6$ (3). A thermogravimetric study has shown that the end of this stage is marked by an inflection point on the TG curve for which the weight loss depends on the grinding time of the sample (15% for 60 min and 27% for 3 min).

In Fig. 3, it can be seen that the diffraction lines of $Ce_2^{III}Rb_3(NO_3)_9$ and *X* vanish simultaneously at about 190°C and that only the lines of CeO_2 are observed from 190 to 210°C. Surprisingly, above 220°C, the diffraction pattern of the tetragonal form of $RbNO_3$ appears suddenly, and the intensity of the lines increases up to 230°C. To explain these observations, TDXD and TG-DSC studies were carried out with successive heating and cooling cycling between 160 and 205°C; the first cycle is displayed in Fig. 4. The DSC curve clearly shows that an endothermic peak on heating and an exothermic peak on cooling are observed, with a maximum at 190°C. From additional thermal cycles, it was observed that the measured enthalpy

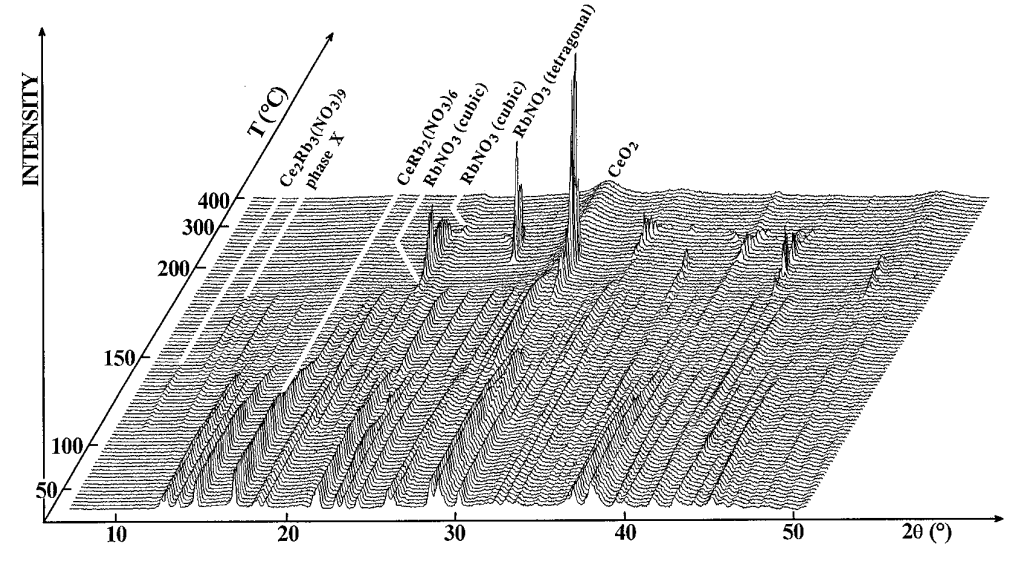

FIG. 6. TDXD plot for $Ce^{IV}Rb_2(NO_3)_6$ milled for 60 min, in vacuum (heating rate: 5°C h^{-1} between room temperature and 110°C, 2°C h^{-1} in the range 110–200°C, and 10°C h^{-1} in the range 200–400°C).

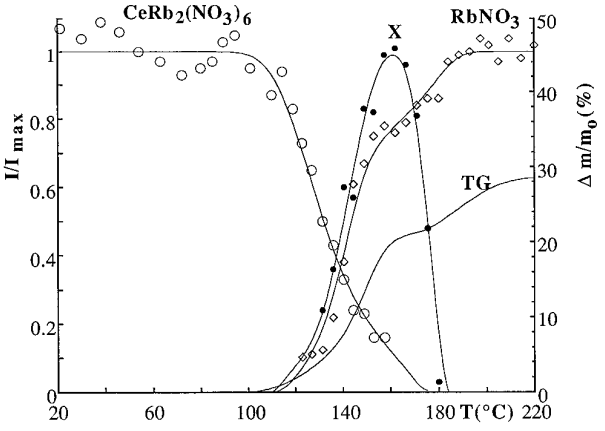

FIG. 7. Integrated intensities of selected diffraction lines vs temperature from the TDXD plot in vacuum, for $Ce^{IV}Rb_2(NO_3)_6$ milled for 13 min. ○, line 011 of $Ce^{IV}Rb_2(NO_3)_6$; ●, the cluster of the two lines at 21.96 and 22.09 (°2θ) of *X*; ◇, line 111 of $RbNO_3$ (hexagonal). The full line represents the TG curve.

change of the transformation increases with the decomposition rate. In addition, as displayed on the corresponding 3D plot, the diffraction lines of *X* vanished above 190°C and appeared again on cooling, below 190°C. Therefore, these results clearly point out that the melting of *X* takes place at 190°C.

In the range 190–220°C, a continuous weight loss is observed, due to the decomposition of the liquid phase obtained. The results described above demonstrate that this decomposition leads to CeO_2 and $RbNO_3$. The fact that the diffraction lines of $RbNO_3$ appear only above 220°C is probably due to a crystallization delay. At higher temperature, $RbNO_3$ melts and undergoes a further complex decomposition (21). The final product obtained is CeO_2.

Thermal Decomposition in Vacuum

The decomposition sequences of the precursor milled for 13 and 60 min are depicted in Figs. 5 and 6, respectively.

TABLE 6
Phases Observed during the Decomposition of $Ce^{IV}Rb_2(NO_3)_6$ Milled for 13 min

Temperature range (°C)	Phases observed
20–125	$Ce^{IV}Rb_2(NO_3)_6$
125–160	$Ce^{IV}Rb_2(NO_3)_6$ + $RbNO_3$ (hexagonal) + CeO_2 + phase *X*
160–190	phase *X* + $RbNO_3$ (hexagonal) + CeO_2
190–220	$RbNO_3$(cubic) + CeO_2
220–280	$RbNO_3$ (tetragonal) + CeO_2
280–400	CeO_2

TABLE 7
Phases Observed during the Decomposition of $Ce^{IV}Rb_2(NO_3)_6$ Milled for 60 min

Temperature range (°C)	Phases observed
20–110	$Ce^{IV}Rb_2(NO_3)_6$
110–145	$Ce^{IV}Rb_2(NO_3)_6$ + $Ce_2^{III}Rb_3(NO_3)_9$
145–175	phase *X*
175–190	$RbNO_3$ (cubic) + phase *X*
190–225	$RbNO_3$ (cubic) + CeO_2
225–290	$RbNO_3$ (tetragonal) + CeO_2
290–310	$RbNO_3$ (cubic) + CeO_2
310–400	CeO_2

Figure 7 exhibits the changes of the integrated intensities with temperature of selected diffraction lines for $Ce^{IV}Rb_2(NO_3)_6$, *X*, and $RbNO_3$ and the corresponding TG curve for the precursor milled for 13 min. The different phases appearing during the processes are summarized in Tables 6 and 7. These results indicate that the decomposition process changes with the mechanical treatment of the precursor. The following features are worth emphasizing:

—The formation of $Ce_2^{III}Rb_3(NO_3)_9$ or the mixture $RbNO_3$–*X*–CeO_2 (Tables 6 and 7), in the first stage of the decomposition, depends on the milling time and, hence, on the microstructure of the precursor. However, the formation of $Ce_2^{III}Rb_3(NO_3)_9$ alone cannot be understood without the formation of $RbNO_3$. Consequently, for the decomposition of the precursor milled for 60 min, $RbNO_3$ behaves like an amorphous phase since its diffraction lines are not displayed on the 3D plot in this first stage (Fig. 6).

—Figure 6 shows that the decomposition of $Ce_2^{III}Rb_3(NO_3)_9$ and $Ce^{IV}Rb_2(NO_3)_6$ ends at approximately the same temperature and that the decomposition product is *X*. Consequently, the question arises as to whether this phase is a cerous or a ceric compound.

—From Fig. 7 it can be seen that about 80% of the total amount of $RbNO_3$ is obtained at the end of the first stage of the decomposition of the precursor milled for 13 min, and that, consequently, *X* provides about 20% of this amount when its decomposes in the second stage. Moreover, the TG curve exhibits an inflection point for which the weight loss is close to 22%. It can be noted that this weight loss depends on the milling time of the precursor (e.g., 17% for a milling time of 60 min, involving the formation of a greater amount of *X*).

—The diffraction lines of *X* vanish at 190°C, which is the melting point *X* as described above.

—During the decomposition of the precursor milled for 60 min (Fig. 6), the diffraction lines of the cubic form of $RbNO_3$ appear at about 175°C and further grow in intensity up to 210°C. This confirms that the liquid phase obtained at 190°C decomposes into CeO_2 and $RbNO_3$. This is sup-

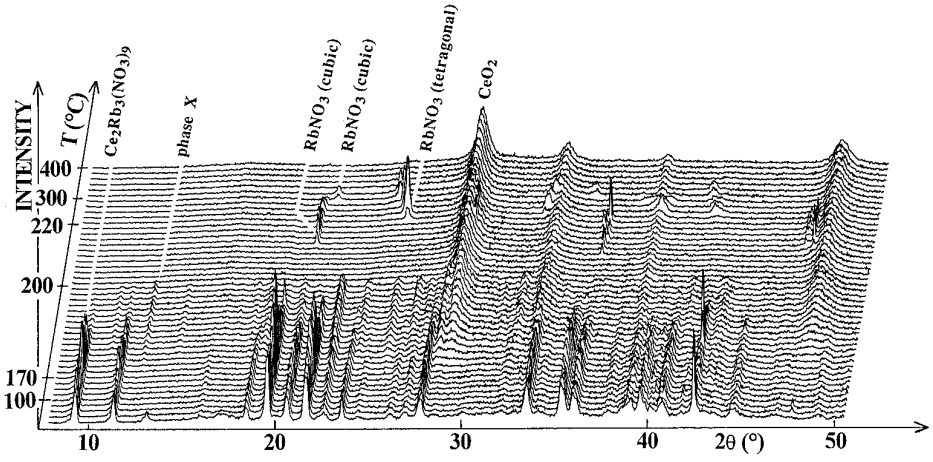

FIG. 8. TDXD plot for $Ce_2^{III}Rb_3(NO_3)_9$, in vacuum (heating rate: 20°C h^{-1} between room temperature and 170°C, 2°C h^{-1} in the range 170–220°C, and 20°C h^{-1} in the range 220–400°C).

ported by the TG curve which shows that the plateau corresponding to the formation of the mixture $RbNO_3$–CeO_2 is only reached at about 210°C.

THERMAL BEHAVIOR OF $Ce_2^{III}Rb_3(NO_3)_9$

From Fig. 8 it can be seen that the first stage of the decomposition of $Ce_2^{III}Rb_3(NO_3)_9$ carried out in vacuum leads to the simultaneous formation of CeO_2 and *X*. Therefore, this feature clearly demonstrates that *X*, found in the decomposition of ceric rubidium nitrate, is finally a cerous compound. Above 195°C, the decomposition sequences are similar to those observed during the decomposition of $Ce^{IV}Rb_2(NO_3)_6$ under nitrogen atmosphere.

The corresponding TG curve shows a continuous weight loss from 180 to 230°C where its value of 28% corresponds to the complete decomposition of the precursor into $RbNO_3$ and CeO_2. Complementary experiments carried out under other experimental conditions did not allow us to obtain a characteristic point at the end of the first stage and, then, to provide any information about the chemical formula of *X*.

CONCLUSION

This study has shown that $Ce^{IV}Rb_2(NO_3)_6$ and $Ce_2^{III}Rb_3(NO_3)_9$ are isostructural with $Ce^{IV}(NH_4)_2(NO_3)_6$ and $Ce_2^{III}K_3(NO_3)_9$, respectively. Their atomic coordinates were refined from their X-ray powder diffraction data. TDXD studies have clearly demonstrated that two mixed cerous nitrates arise from $Ce^{IV}Rb_2(NO_3)_6$ upon heating and, consequently, that the Ce(IV) → Ce(III) → Ce(IV) reduction–oxidation sequence appears again in the decomposition scheme of a ceric alkaline nitrate. The first cerous phase is $Ce_2^{III}Rb_3(NO_3)_9$. The second is an intermediate phase in the thermal decomposition of this last cerous compound. Its chemical formula, $Ce^{III}Rb(NO_3)_4$, may be suggested from TG and TDXD results obtained for the decomposition of the precursor milled for 13 min in vacuum. This compound melts at about 190°C and undergoes a subsequent decomposition into $RbNO_3$ and CeO_2. Its

TABLE 8
X-ray Powder Diffraction Data for $Ce^{III}Rb(NO_3)_4$

d_{obs} (Å)	I_{obs}
8.54	15
8.11	11
7.77	6
7.30	15
6.36	9
5.25	14
5.01	10
4.838	23
4.793	37
4.593	6
4.438	13
4.418	17
4.258	8
4.043	34
4.020	53
3.791	45
3.731	5
3.569	19
3.553	29
3.405	40
3.319	16
3.272	24
3.211	100

powder diffraction pattern is given in Table 8. The accuracy of these data is low due to significant line broadening and indexing attempts were unsuccessful.

Depending on the mechanical treatment of the precursor and the environmental atmosphere used, the Ce(IV) → Ce(III) reduction sequence can take place through a process involving the formation of one of the following mixtures of phases:

$Ce_2^{III}Rb_3(NO_3)_9$–$Ce^{III}Rb(NO_3)_4$–CeO_2 (under nitrogen, sample milled for 21 min);

$RbNO_3$–$Ce^{III}Rb(NO_3)_4$–CeO_2 (under vacuum, sample milled for 13 min);

$Ce_2^{III}Rb_3(NO_3)_9$–amorphous $RbNO_3$ and then $Ce^{III}Rb(NO_3)_4$–amorphous $RbNO_3$–CeO_2 (under vacuum, sample milled for 60 min).

This study points out that the double valence change of cerium occurs not only during the decomposition of $Ce^{IV}K_2(NO_3)_6$, but also during that of $Ce^{IV}Rb_2(NO_3)_6$. It is obvious that the redox reaction taking place during the first stages of the decomposition can only proceed through the oxidation of the oxygen atom of the nitrate groups by the Ce^{4+} cation as previously described (3). The question arises as to whether this phenomenon can be expected for all the mixed ceric nitrates $Ce^{IV}M_2(NO_3)_6$, where M is a monovalent cation. The present investigation has shown that the decomposition process grows in complexity from the potassium to rubidium salts. Moreover, the thermal behavior of $Ce^{III}Cs_2(NO_3)_6$ would certainly be worth an investigation by means of TDXD analysis. This study would allow one to complement the results obtained by Pokol *et al.* (8) who, from magnetic susceptibility measurements carried out *ex situ,* have shown that cerium preserves the +4 oxidation state throughout the thermal decomposition.

REFERENCES

1. G. F. Smith, V. R. Sullivan, and G. Frank, *Ind. Eng. Chem.* **8**(6), 449 (1936).
2. N. Guillou, Thesis, University of Rennes I, July 5, 1994.
3. N. Guillou, J. P. Auffrédic, and D. Louër, *J. Solid State Chem.* **115,** 295 (1995).
4. S. A. Bondar', N. L. Nikhailova, R. A. Popova, and S. D. Nikitina, *Zh. Neorg. Khim.* **31,** 625 (1986); *Russian J. Inorg. Chem* (*Engl. Transl.*) **31,** 356 (1986).
5. J. B. Sharma, V. Singh, and M. Lakhanpal, *J. Thermal Anal.* **42,** 343 (1994).
6. Y. Ying and Y. Rudong, *Thermochim. Acta.* **202,** 301 (1992).
7. S. A. Bondar', G. V. Trofimov, R. A. Popova, and L. S. Korobeinikov, *Izv. Akad. Nauk SSR, Neorg. Mater.* **18,** 1209 (1982); *Inorg. Mater.* (*Engl. Transl.*) **18,** 1019 (1982).
8. G. Pokol, T. Leskelä, and L. Niinistö, *J. Thermal Anal.* **42,** 343 (1994).
9. N. Guillou, M. Louër, J. P. Auffrédic, and D. Louër, *Eur. J. Solid State Inorg. Chem.* **32,** 35 (1995).
10. N. Guillou, J. P. Auffrédic, M. Louër, and D. Louër, *J. Solid State Chem.* **106,** 295 (1993).
11. R. J. Meyer and R. Jacoby, *Z. Anorg. Chem.* **27,** 359 (1901).
12. D. Louër and J. I. Langford, *J. Appl. Crystallogr.* **21,** 430 (1988).
13. J. Plévert, J. P. Auffrédic, M. Louër, and D. Louër, *J. Mater. Sci.* **24,** 1913 (1989).
14. A. Boultif and D. Louër, *J. Appl. Crystallogr.* **24,** 987 (1991).
15. A. D. Mighell, C. R. Hubbard, and J. K. Stalick, "NBS*AIDS80: A FORTRAN Program for Crystallographic Data Evaluation." NBS (U.S.) Tech. Note 1141. [NBS*AIDS83 is an expanded version of NBS*AIDS80]
16. T. A. Beineke and J. Delgaudio, *Inorg. Chem.* **7,** 715 (1968).
17. N. Guillou, M. Louër, J. P. Auffrédic, and D. Louër, *Acta Crystallogr. Sect. C* **51,** 1029 (1995).
18. N. Guillou, J. P. Auffrédic, and D. Louër, *Acta Crystallogr. Sect. C* **51,** 1032 (1995).
19. J. Rodriguez-Carvajal, *in* "Collected Abstract of Powder Diffraction Meeting," p. 127. Toulouse, France 1990.
20. C. C. Addison, N. Logan, S. C. Wallwork, and C. D. Garner, *Q. Rev.* **25,** 289 (1971).
21. C. C. Addison and N. Logan, *Adv. Inorg. Chem. Radiochem.* **6,** 72 (1964).